



Bimetal MOF derived mesocrystal $ZnCo_2O_4$ on rGO with High performance in visible-light photocatalytic NO oxidization

Shuning Xiao^{a,c}, Donglai Pan^b, Rui Liang^b, Wenrui Dai^{c,e}, Qitao Zhang^a, Guoqiang Zhang^{a,c}, Chenliang Su^{a,*}, Hexing Li^{b,*}, Wei Chen^{c,d,e,**}

^a SZU-NUS Collaborative Innovation Center for Optoelectronic Science & Technology, International Collaborative Laboratory of 2D Materials for Optoelectronics Science and Technology of Ministry of Education, College of Optoelectronic Engineering, Shenzhen University, Shenzhen 518060, China

^b International Joint Laboratory of Resource Chemistry SHNU-NUS-PU, Department of Chemistry, Shanghai Normal University, Shanghai 200234, China

^c Department of Chemistry, National University of Singapore, 3 Science Drive 3, 117543, Singapore

^d Department of Physics, National University of Singapore, 2 Science Drive 3, 117542, Singapore

^e National University of Singapore (Suzhou) Research Institute, 377 Lin Quan Street, Suzhou Industrial Park, Jiangsu 215123, China



ARTICLE INFO

Keywords:

Environmental catalysis

NO oxidation

MOF

rGO

Photocatalysis

ABSTRACT

A mesocrystal $ZnCo_2O_4$ on reduced graphene oxide (rGO) nano-composite was successfully synthesized by a low-temperature annealing of bimetal organic frameworks on rGO. In this nano-composite, rGO nanosheets worked as the two-dimensional support to significantly improve the dispersity and conductivity of nano-composites. The mesoporous $ZnCo_2O_4$ crystal derived from ZnCo-ZIF worked as the main active sites with the optimized Zn/Co ratio to ensure an ideal valence band structure as well as enhanced visible-light harvesting properties. The as-prepared rGO@ $ZnCo_2O_4$ nano-composites showed a remarkable activity in visible-light photocatalytic NO oxidation with the conversion of 83.8% under visible light and 92.6% under simulated solar light. It also exhibited a higher stability than that of N-doped TiO_2 , thereby making this nano-composite as a promising and stable photocatalyst for environmental remediation.

1. Introduction

The concentrations of nitrogen oxide (NO_x) in the atmosphere are continuously increasing due to the springing growth of the industrial development and automobile exhausting. It can even cause severer secondary pollutions, such as photochemical smog, acid rain, $PM_{2.5}$ and other serious environmental problems to the human health [1]. Among the NO_x , nitric oxide (NO) accounts for about 95% of the total emission. After entering into the air, NO can react with O_2 to produce a series of NO_x due to the highly reactive chemical properties. Therefore, the effective removal of NO before its conversion is particularly important for the health security and sustainable economic development of modern society [2]. During the past few decades, different routes, such as selective catalytic reduction (SCR) [3–9], selective non-catalytic reduction (SNCR) [10–12], and photocatalytic technologies have been explored for removing NO. Among them, the photocatalytic route [13–16] have attracted substantial attentions due to its preferred advantages, including simple operation, mild reaction condition, low cost, high efficiency, and good durability [17].

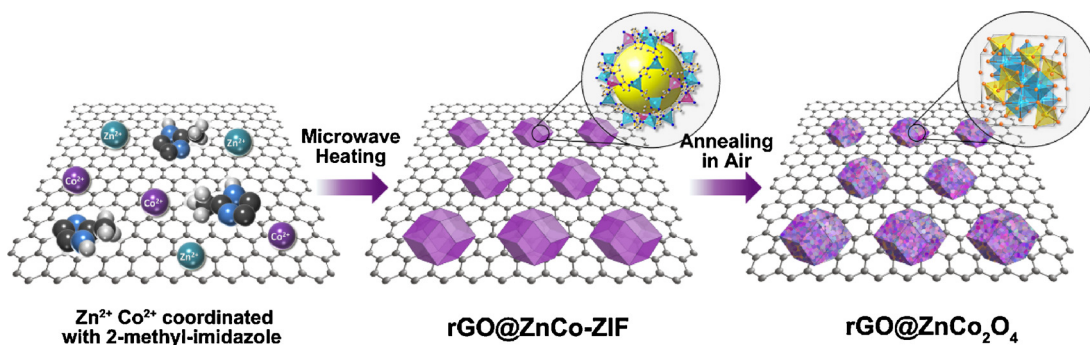
TiO_2 is the most commonly used semiconductor photocatalysts for

NO oxidation since its highly positive valence band position that makes it possible for photo-excited holes to oxide NO directly [18–22]. However, the rapid recombination rate of photo-excited electron-hole pairs as well as the merely UV-response restricts its more extensive application in the practical low-concentration NO removal. Numerous catalysts-design strategies have been developed to solve these issues, such as co-catalyst with noble-metals [23–25], ions doping [26–28], composited with carbon materials [29–31] and other semiconductors [32–34]. On the other hand, novel visible-light driven photocatalysts are gradually developed for this reaction, like $g-C_3N_4$ [35,36], Bi-based semiconductors [37–40] and so on. Recently, metal organic frameworks (MOF) and their derivatives have become one of the most attractive series of functional materials that can be widely utilized in energy storage [41–43], gas storage and absorption [44–46], electro-catalysis [47–49] as well as photocatalysis [50–52] due to their large surface area, controllable functional groups and uniform pore size. For mild photocatalytic gas-phase reaction, MOF-based materials can retain their pore structures under the reaction environment, and of utmost significance, such special structure shows excellent adsorption ability with great potential for gas-phase catalysis. However, to the best of our

* Corresponding authors.

** Corresponding author at: Department of Chemistry, National University of Singapore, 3 Science Drive 3, 117543, Singapore.

E-mail addresses: chmsuc@szu.edu.cn (C. Su), hexing-li@shnu.edu.cn (H. Li), phycw@nus.edu.sg (W. Chen).



Scheme 1. Schematic illustration the formation of the rGO@ZnCo₂O₄ hybrid with hierarchical structure.

knowledge, only Ag doped MIL-125-like MOF was used as catalyst for NO oxidation with limited stability [53], possibly due to the limited electron conductivity and the less utilized inner surface in microporous structures for MOF-based materials. Therefore, to be used for the gas-phase NO oxidation reaction, it is highly desirable to improve the porous structure, conductivity and the stability for the MOF and their derivative materials.

Herein, we reported a novel MOF-derived nano-composite for visible-light driven NO oxidation reaction, comprising the reduced graphene oxide (rGO) nanosheets as the two-dimensional (2D) support with the loaded mesoporous ZnCo₂O₄ crystal as semiconductor photocatalyst. Scheme 1 showed the formation of the rGO@ZnCo₂O₄ hybrids with hierarchical structure. As illustrated, after ultrasonication in methanol, the abundant hydroxyl and carbonyl functional groups on the surface of the well dispersed GO could strongly bind with metal ions (Zn²⁺ and Co²⁺). Meanwhile, the 2-methyl-imidazole ligands could also be attracted by the benzene rings from GO via noncovalent π - π interactions. After that, upon irradiated by the microwave, the GO with strong electromagnetic-to-heat conversion ability could be induced to form a super-hot surfaces. It resulted in the rapid nucleation and gradual growth of ZnCo-ZIF dodecahedron crystals on GO. In addition, with the thermal reduction property of the solvent, the GO could be reduced to rGO. Finally, by annealing the as-prepared rGO@ZnCo-ZIF in air at 300 °C, the ZnCo-ZIF crystals were oxidized to form ZnCo₂O₄ with the morphology changing to the mesoporous with retained frameworks in the shape of rhombic dodecahedron. Such unique nano-architecture of rGO@ZnCo₂O₄ hybrid could benefit from the synergistic effects of each component to meet the critical requirements for high-performance photocatalytic air purification, including (1) the ZnCo₂O₄ mesocrystals could effectively favor the gas pollutant absorption; (2) the in-situ growth leads to an intimate contact between the ZnCo₂O₄ mesocrystals and the rGO nanosheets to improve the hybrids conductivity and to further create an interconnected electron transport percolation network for the photo-excited carriers; (3) the optimized Zn/Co ratio in the crystal can result in a suitable valence band structure with enhanced visible-light harvesting properties, further improving the photocatalytic activities. As a result, the as-prepared rGO@ZnCo₂O₄ nano-composite represents a promising visible-light driven photocatalyst with an improved gas pollutant removal efficiency and long-term stability.

2. Experimental

2.1. Synthesis of rGO@ZnCo-ZIF composites

In a typical synthesis, 50 mg of graphene oxides (GO, 0.2–10 μ m in average diameters, Shanghai Ashine Technology Development Co., Ltd.) were dispersed in 20 mL of methanol under ultrasonication for 30 min. Then 8 mmol of 2-methylimidazole (H-Mim) was slowly added into the GO dispersion with continuous magnetic stirring to form solution A. To form solution B, 4 g of polyvinylpyrrolidone (PVP, Mw ~55,000) and a

certain ratio of Zn(NO₃)₂·6H₂O and Co(NO₃)₂·6H₂O with total molar of 2 mmol were added into 20 mL of methanol by ultrasonication for 30 min. After that, with continuous stirring, solution B was added dropwise into solution A. The mixture was then transferred into a 60 mL of double-walled Teflon-lined microwave reaction vessel in high-pressure microwave synthesis system (Ethos ONE, Milestone). It was then heated at a heating rate of 10 °C min⁻¹ to 140 °C and was kept at this temperature for 30 min. After being cooled down to room temperature, as-synthesized samples were washed thoroughly with methanol and ethanol for 3 times and dried at 0 °C in a low-temperature vacuum drier. By adjusting the amount of Zn(NO₃)₂·6H₂O and Co(NO₃)₂·6H₂O, we got different samples with the Zn/Co molar ratios in the order of 2.0, 1.5, 1.0, 0.75 and 0.50, respectively. For convenience, the Gr-ZnCo-ZIF-1.0 sample was abbreviated as Gr-ZnCo-ZIF. In addition, Gr-ZIF67 and Gr-ZIF8 were synthesized with only adding one metal (Co and Zn, respectively) into the precursors. Sample ZnCo-ZIF was obtained by similar approach without the addition of GO in solution A.

2.2. Synthesis of rGO@ZnCo₂O₄ composites

The rGO@ZnCo₂O₄ composites were synthesized from the Gr-ZnCo-ZIF. In a typical synthesis, 200 mg of the as-prepared sample Gr-ZnCo-ZIF was placed on the bottom of a quartz boat. Then, it was heated to 300 °C in a tube furnace with 10 °C min⁻¹ heating rate under 200 sccm airflow. After holding at a certain temperature for 3 h, the rGO@ZnCo₂O₄ sample was obtained. With adjusting annealing temperature for Gr-ZnCo-ZIF of 100, 200, 300, 400 and 500 °C, as-synthesized samples were labeled as GZC-100, GZC-200, GZC-300, GZC-400 and GZC-500. For comparison, GC-300, GZ-300 and ZC-300 were synthesized by the similar annealing approach of samples Gr-ZIF67, Gr-ZIF8 and ZnCo-ZIF, respectively. GZC-300-MX was the mechanical mixture of rGO and ZC-300.

2.3. Characterization

The crystal phase was determined by X-ray diffraction (XRD, Rigaku Ultima IV Cu-K α). Materials morphologies were characterized on a transmission electron microscopy (TEM, JEOL, 2010 F) and a field scanning electron microscopy (FESEM, HITACHI, S-4800). The high-angle annular dark-field scanning transmission electron microscopy HAADF-STEM was recorded by using FEI Tecnai G2 F20 TEM, 200 kV. The energy-dispersive X-ray spectroscopy (EDX) element mapping signals was recorded and analyzed by Oxford X-Max^N 100TLE SDD detector installed at FEI Tecnai TEM instrument. Materials surface electronic states were collected by X-ray photoelectron spectroscopy (XPS, Thermo Fisher Scientific, ESCALAB 250Xi, Al-K α). All the binding energy values were calibrated by using C1 s = 284.6 eV as a reference. The specific surface area (S_{BET}), pore volume (V_p) were tested by nitrogen adsorption and desorption isotherm and calculated by applying Brunauer–Emmett–Teller (BET) models on desorption branches (Micromeritics, TriStar II 3020).

2.4. Photoelectrochemical measurement

The photocurrents and electrochemical impedance spectroscopy (EIS) measurements were carried out in a conventional three-electrode, single-compartment quartz cell on an electrochemical station (CHI 660E). Samples with an active area of ca. 4.0 cm² on an ITO glass were served as working electrode. The counter electrode and the reference electrode were platinum sheet and saturated calomel electrode (SCE), respectively. A bias voltage of 0.20 V was utilized to drive the photo-generated electrons transfer. A 3 W LED lamp with central wavelength of 420 nm located at 10 cm away from the photoelectrochemical cell was used as light source. A 0.50 M Na₂SO₄ aqueous solution was used as the electrolyte. The EIS tests were carried out at the bias of the open circuit voltage and recorded over a frequency ranged from 0.1 to 10⁵ Hz with AC amplitude of 10 mV.

2.5. Photocatalytic NO oxidation

As is shown in Fig. S1, the photocatalytic NO oxidation in gas phase was carried out at ambient temperature in a continuous flow reactor with volume of 10.8 L (36 × 20 × 15 cm). Two 150 W of halogen lamps were used as the solar light sources. The visible light photocatalytic reaction was carried with a UV cut filter to cut off lights with the wavelength < 420 nm. In each run of experiment, an ultrapure air gas flow containing 500 ppb NO was allowed to pass through 0.20 g of photocatalyst at the rate of 4.0 L/min. After reaching adsorption-desorption equilibrium on the photocatalyst, the lamps were turned on to start the photocatalytic reaction. The concentration of NO was continuously measured by the chemiluminescence NO analyzer (Thermo Environmental Instruments Inc. Model 42i). The NO removal ratio (%) was calculated based on the following equation: NO conversion (%) = (C₀ - C)/C₀ × 100%, where C₀ and C refer to the NO concentration determined before and after the reaction.

The active species trapping experiments were performed with the trapping agents of AgNO₃ for e⁻, KI for h⁺, p-benzoquinone (PBQ) for O₂⁻ and tert-butyl alcohol (TBA) for ·OH. Typically, different agents were dissolved in 20 mL of ethanol by stirring. Then, 0.20 g of the photocatalysts were added and ultra-sonicated for 10 min to form a uniform suspension. After that, the suspension was evenly spread onto two glass petri dishes and was dried at 60 °C under vacuum for further use. The photocatalytic NO oxidation activities of species trapped samples were tested similar to the method as mentioned above.

3. Result and discussion

The Gr-ZnCo-ZIF precursor was synthesized according to the solvothermal method as previously reported with some modification [54]. After irradiated under high-frequency electromagnetic wave in methanol, the GO can be reduced to rGO with the formation of much more isolated and exfoliated layers as revealed in Fig. 1a and d [55–58]. Fig. 1a and d also showed the rhombic dodecahedron shape of ZnCo-ZIF precursor with an average single crystals size of ~150 nm and was uniformly dispersed onto the wrinkled rGO. By comparing with literatures [59–61], our ZnCo-ZIF showed a much smaller size, which could be attributed to two main reasons. Firstly, rapid microwave heating successfully reduced the reaction time by the strong absorber GO, which initiated faster nucleation and growth of ZIF crystal. Secondly, nano-sized carbon materials (eg. CNTs, graphene) could effectively confine the crystal growth by the steric effect in three-dimensional topological space. Fig. 1b and 1e showed the SEM and TEM images of the composite sample after calcination at 300 °C. No obvious morphology changes could be noticed in the layered structure of rGO by the low-temperature calcination that we had discussed in previous work [62]. Thus, the high electrical conductivity of 2D rGO nanosheets could be retained in the hybrids and could facilitate the charge transport during the photocatalytic reaction. On the contrast, the ZIF crystals

transformed into porous rhombic dodecahedrons due to the oxidation process, where the oxygen replaced part of H-mim organic ligands. Thanks for the low annealing temperature as well as the protection by rGO, the particle sizes of crystal remained as ~150 nm in diameter without any obvious aggregation or destruction. However, further increasing annealing temperature to 500 °C leaded to the burning out of the graphene nanosheets since no layered structure of rGO could be observed in neither SEM nor TEM images in Fig. 1c and f. In addition, the dodecahedron frameworks were shrunk dramatically with the formation of graphite like structure and aggregation of metal oxides crystals.

In order to understand the annealing products, the X-ray diffraction measurement was conducted. As illustrated in Fig. 2a, as prepared Gr-ZnCo-ZIF presented well crystalline diffraction peaks, which were in excellent agreement with that of both ZIF-67 and ZIF-8 due to the very similar lattice parameters. After calcination, the peaks of ZIF disappeared accompanied with new peaks appeared at 2θ of 19.0°, 31.2°, 36.8°, 38.5°, 44.7°, 49.0°, 59.3° and 65.1°. They can be indexed to the (111), (220), (311), (222), (400), (331), (511) and (440) planes of cubic ZnCo₂O₄ (PDF #23-1390) with spinel group isometric system. Due to the small crystal size and the weak crystallinity, the peaks of ZnCo₂O₄ did not seem very sharp in sample GZC-300 than that of GZC-500 sample. Nitrogen adsorption and desorption isotherm was carried out to study the surface area and pore volume of different samples. As shown in Fig. 2b, the Gr-ZnCo-ZIF sample displayed a type I isotherm with a large surface area of 1402 m²/g, which mainly arose from micropores in ZIF crystal determined by the space of metal-ligand coordination. Unfortunately, this kind of pores could not be fully utilized in gas-phase photocatalysis since the light could hardly irradiate into the micropores to excite semiconductors inner surfaces. On the contrast, after annealing, the GZC series sample exhibited type IV isotherm with mesoporous structure, which was suitable for gas reactant adsorption and light transmission. By BET method calculation, the surface area of GZC-300 and GZC-500 were 892 m²/g and 407 m²/g, respectively. The decrease surface area for GZC-500 sample was mainly owing to the loss of graphene support and the aggregation of crystals.

TEM images in Fig. 3(a) and (b) further confirmed the uniform distribution of ZnCo₂O₄ dodecahedron crystals onto rGO nanosheets. In Fig. 3(c), clear mesopores could be noticed obviously inside the ZnCo₂O₄ crystals that is consistent with the BET results. The HRTEM in Fig. 3e revealed two crossed lattice spacing of ca. 0.216 nm and 0.330 nm with the angle of 102.6° between them, which were corresponded to the (-1-2) and (112) planes of spinel ZnCo₂O₄ single crystals. The selected area electron diffraction (SAED) pattern in the insert was captured from the [-804] axis. Since only single spots diffraction appeared in the pattern, the as-prepared ZnCo₂O₄ should be classified to the single crystal. By analyzed the set of spots in parallelogram near the diffraction center according to the crystal parameters from cubic ZnCo₂O₄ (PDF #23-1390), the selected three crystal planes could be indexed to (112), (040) and (-13-2) respectively, which was corresponded to the HRTEM results shown in Fig. 3e. The as-prepared ZnCo₂O₄ possessed the mesoporous structure and single crystal in nature, and hence referred to as the mesocrystal. In addition, the surface compositions of the hybrid nanocomposites were investigated by HAADF-STEM and EDX as shown in Fig. 3(d) and (f)–(j). The selected area elements mapping images of C, O, N, Zn and Co in GZC-300 depicted the uniform distribution of Zn, Co and O elements on the rGO nanosheets. As noticed in EDX spectra shown in Fig. S2, the weak intensity of the N-k signal in GZC-300 revealed the transformation from ZIF to metal oxide of the crystal after annealing.

The optical properties of GZC-300, GZ-300, GC-300 and Gr-ZnCo-ZIF were compared by UV-vis diffuse reflectance spectra as shown in Fig. 4a. The entire four samples showed a gradually elevated absorbance in the visible light region, which could attribute to the dark color of graphene [55,63]. The Gr-ZnCo-ZIF precursor exhibited a strong absorption edge at approximately 336 nm ascribed to the characteristic

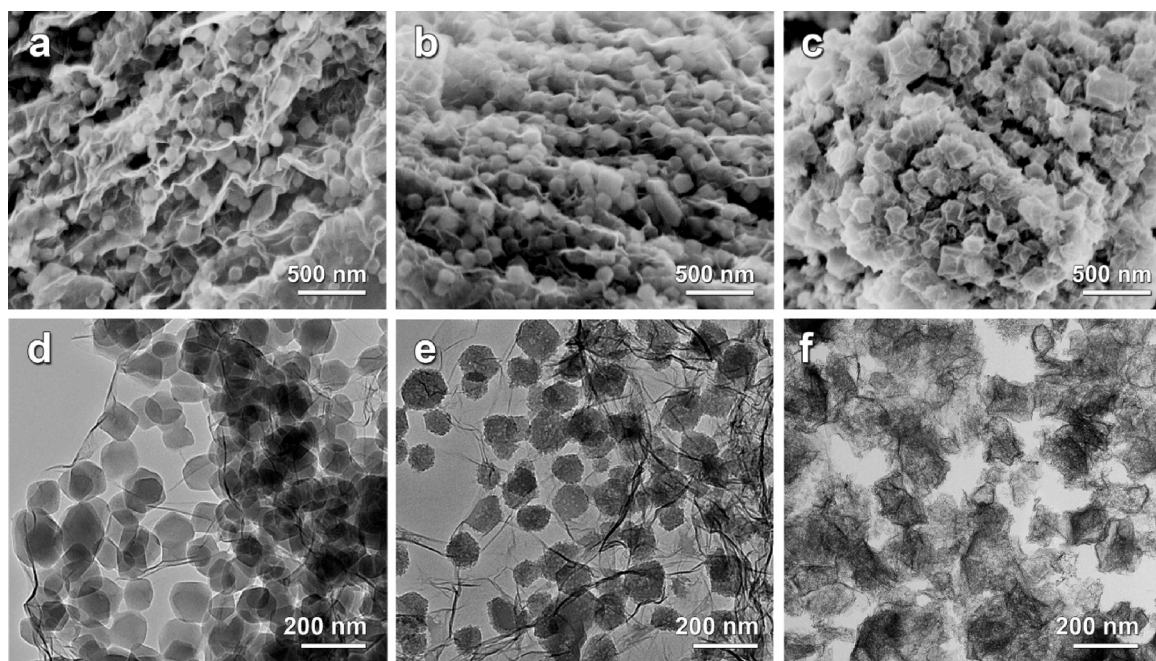


Fig. 1. The morphologies of as-prepared composite materials with the SEM images of (a) Gr-ZnCo-ZIF, (b) GZC-300, (c) GZC-500 and the TEM images of (d) Gr-ZnCo-ZIF, (e) GZC-300, (f) GZC-500.

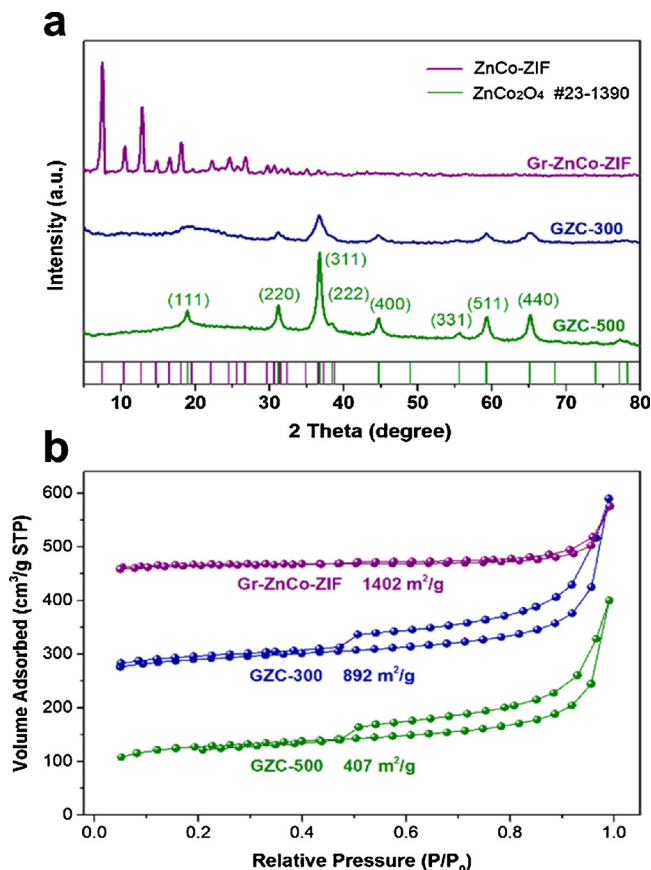


Fig. 2. (a) The XRD patterns and (b) nitrogen adsorption and desorption isotherm of as-prepared Gr-ZnCo-ZIF, GZC-300 and GZC-500.

absorption of ZnCo-ZIF. The annealed three samples presented different absorption edge: 340 nm for GZ-300, 510 nm for GC-300 and 460 nm for GZC-300, respectively. For GZ-300, it was similar to the optical property of ZnO with only UV response, [58,64] since the oxidation

product of ZIF-8 was ZnO as confirmed by XRD in Fig. S3. While the visible-light response of GC-300 could be identified to the instinct light response of Co₃O₄ [65,66] (XRD result shown in Fig. S4). Since both Zn and Co could affect the band structure of semiconductors [67,68], the GZC-300 exhibited combined optical properties between the above two samples, which corresponded to a calculated band gap of 2.7 eV by Kubelka-Munk transformation in Fig. 4b. Interestingly, in the three of Co-contained samples, there existed two distinct peaks at 540 and 590 nm along with a shoulder at 567 nm. They could be defined as cobalt in tetrahedral coordination with other ligands, but had little effect to visible-light photocatalysis [69]. Compared with GZ-300 and Gr-ZnCo-ZIF, the stronger light absorption and suitable band gap of GZC-300 would lead to the more efficient utilization of visible light energy, thus it might possess better visible-light driven photocatalytic activity.

In order to determine the element valence and chemical bonding state before and after annealing, the XPS measurement was carried out and analyzed. As illustrated in Fig. 5a, both GZC-300 and Gr-ZnCo-ZIF presented two sharp peaks in 1044.8 eV and 1021.6 eV, corresponding to the signals from Zn²⁺ 2p_{1/2} and Zn²⁺ 2p_{3/2} core levels, respectively since Zn²⁺ had a stable oxidation state by loss of two electrons from the 4s orbital. However, after calcined, the oxidation state of Co changed obviously as shown in Fig. 5b. The peaks with binding energies at 781.8 eV and 780.0 eV of Co 2p_{3/2} could be indexed as Co³⁺ and Co³⁺, respectively as well as one satellite peak was fitted. After the oxidation reaction in air with the annealing temperature of 300 °C, the ratio of Co³⁺/Co²⁺ significantly increased by comparing the peak area of Co²⁺ and Co³⁺. In addition, the N 1s high-resolution XPS spectra of GZC-300 (Fig. 5c) revealed the four chemical states: N-metal bonds, pyridinic N, pyrrolic N and oxidized N, where the binding energies were 399.6 eV, 398.7 eV, 400.6 eV and 402.9 eV, respectively. In comparison, with the typical property of imidazole MOF materials, the Gr-ZnCo-ZIF sample showed only two fitted chemical states of N-metal bonds and pyridinic N. The formation of pyrrolic N and oxidized N in sample GZC-300 could be attributed to the rearrangement of C and N atoms and combination with O by temperature increasing. At last, the O 1s peaks in the both samples exhibited three oxygen states of O²⁻ at 530.9 eV, O⁻ at 531.8 eV and *O at 532.8 eV (Fig. 5d). The O²⁻ was originated from the

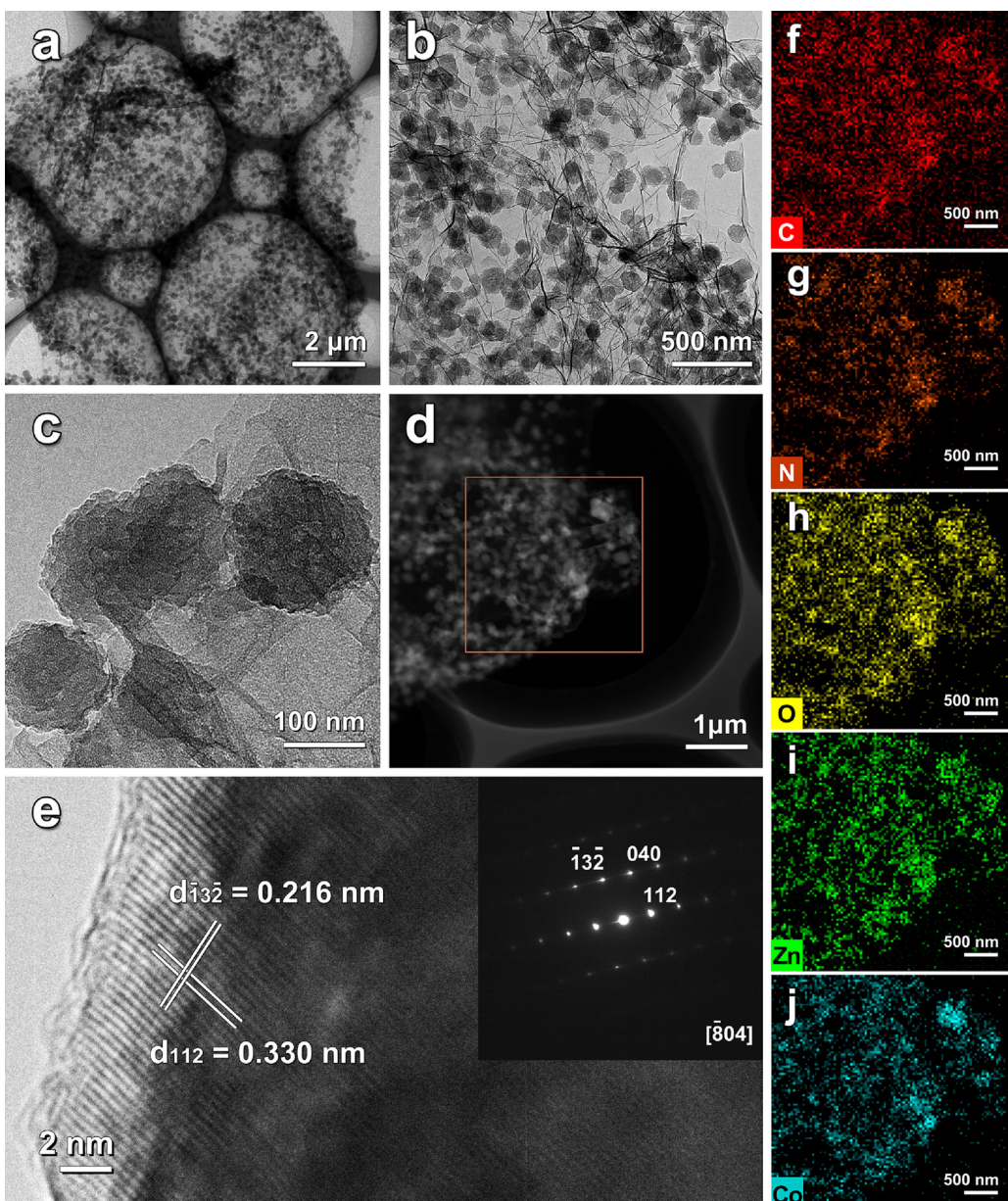


Fig. 3. (a)(b)(c) TEM images of GZC-300 of different scales. (d) HAADF-STEM image and element mapping images of (f) C-k, (g) N-k, (h) O-k, (i) Zn-k, and (j) Co-k of GZC-300 based on the selected area in HAADF-STEM. (e) HRTEM image of sample GZC-300 with the SAED pattern in the insert.

typical metal–oxygen bonds, while O- was associated the chemically adsorbed oxygen or uncoordinated oxygen and $^{*}\text{O}$ came from the physically adsorbed water. It was noted that, in Gr-ZnCo-ZIF precursor, the O element mainly consisted of Zn/Co-O bonds and the physically adsorbed O, which is due to the internal lattice structure and the large surface area of MOF materials. In GZC-300, the calcination process resulted in the increasing of O^{2-} and O- by the break of Zn/Co-N bonds with a considerable amount and the following formation of new Zn/Co-O bonds as well as uncoordinated oxygen.

The visible-light driven NO oxidation was utilized as a probe reaction to evaluate the photocatalytic performance of the as-prepared rGO@ZnCo₂O₄ nano-composites. As the main product of NO oxidation is proved as NO_3^- according to literature reported before, we could use the NO conversion to indicate its removal [18–22]. (The experimental recorded concentration of NO/NO₂/NO_x during the photocatalysis was given in Fig S5) As shown in Fig. 6a, the GZC-300 exhibited the highest NO conversion of 83.8% among the five samples. With the similar BET surface area of GZC-300 (nitrogen adsorption and desorption isotherm

of GZ-300 and GC-300 were shown in Fig. S6), the GZ-300 sample prepared by only Zn^{2+} added showed trace photocatalytic activity owing to the its wide band gap, which could not be excited by visible light (confirmed by the UV-vis spectra in Fig. 4a). Despite its good optical properties, the GC-300 sample prepared by only Co^{2+} exhibited a much lower activity with about 1/4 of the NO conversion of GZC-300. It was attributed to the decreased oxidizability since the GC-300 had the much more negative valence band energy than that of GZC-300. ZC-300 was the sample without adding GO during the synthesis. It displayed a higher activity than that of both GZ-300 and GC-300 with 26.7% conversion after 10 min's light irradiation, but gradually dropped to 15.2% in 60 min because the lack of rGO resulted in the high recombination of photo-excited electron and holes. The mechanical mixing ZC-300 and rGO (GZC-300-MX) regained some of this activity by reaching nearly the doubled NO conversion of ZC-300 since the rGO nanosheets facilitated electron transfer and hence reduced their recombination with holes to a certain degree. However, its activity was still remarkably lower than that of the *in-situ* synthesized GZC-300

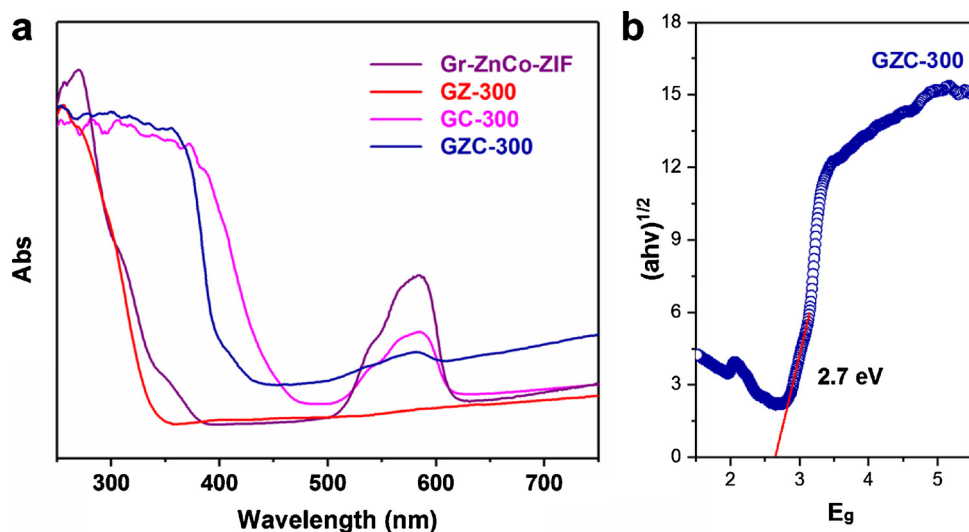


Fig. 4. (a) UV-vis diffuse reflectance spectra of sample Gr-ZnCo-ZIF, GZ-300, GC-300 and GZC-300, (b) calculated band gap energies of samples GZC-300 by Kubelka-Munk transformation.

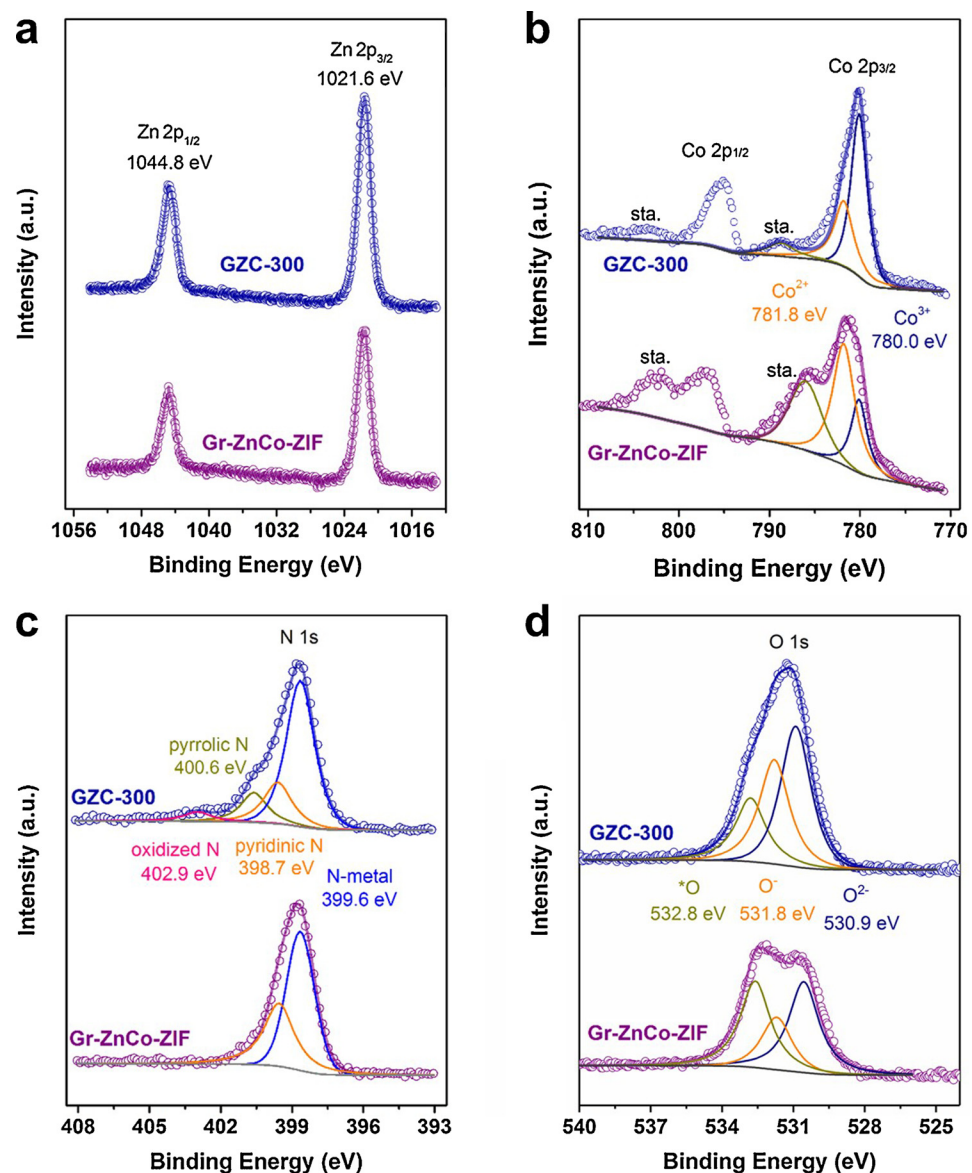


Fig. 5. The high-resolution XPS spectra of sample GZC-300 and Gr-ZnCo-ZIF: (a) Zn 2p, (b) Co 2p, (c) N 1s and (d) O 1s.

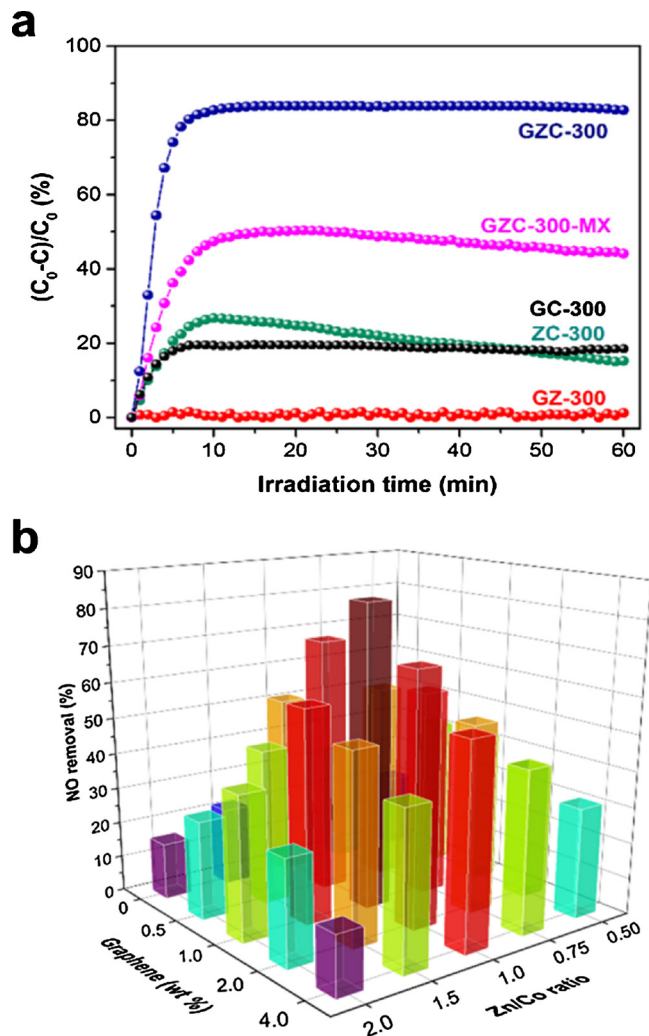


Fig. 6. (a) Reaction profiles of photocatalytic NO oxidation under visible light ($\lambda \geq 420$ nm) irradiation, (b) two parameters materials optimization.

because of the weak interaction of ZnCo_2O_4 with rGO, which could be confirmed by the EIS comparison shown in Fig. 7a. The radius of the semicircles on the Nyquist plot reflected the conductivity, charge transfer and carrier recombination kinetics during the photocatalytic process. Among the three samples, the GZC-300 displayed the smallest semicircle corresponding to the best conductivity and charge transport

ability. Photocurrent measurement was carried out as shown in Fig. 7b with the intensity increased in the order of GZ-300, ZC-300, GC-300, GZC-300-MX and GZC-300. It was well coincident with the NO oxidation results. Taking into account their large difference in light absorbance, this result could be ascribed to the synergistic effect by their electron-hole recombination as well as the light absorbance. After noticing the advantages of rGO and the Zn/Co bimetallics, we had adjusted the two parameters of both rGO amount (0, 0.5, 1.0, 2.0 and 4.0 wt%) and the molar ratio of Zn/Co (2.0, 1.5, 1.0, 0.75 and 0.50) during the synthesis for catalytic performance optimization. As shown in Fig. 6b, by testing the visible-light driven photocatalytic activity of all the 25 (5×5) samples, the catalyst with 1.0 wt% of rGO and with 1.0 of Zn/Co molar ratio exhibited the highest NO conversion. According to the energy gap of ZnO , Co_3O_4 and ZnCo_2O_4 , we could clearly understand why the Zn/Co ratio was such important for the NO oxidation. As well known, ZnO had the most positive valence band (VB) position among the three semiconductors, thus the photo-excited holes could easily oxidize NO directly, but it failed to be excited by the visible light. On the contrast, the Co_3O_4 with the most narrowed band gap should have the best visible light activity, but the more negative VB position had no enough energy to oxidize NO directly, thus resulting in the low activity. Only by well balancing the band gap and VB position through adjusting the Zn/Co ratio, could it reach the high NO removal under visible light irradiation.

For these bimetallic MOF derived composite photocatalysts, annealing temperature could also affect their performances significantly by changing their surface states, chemical components as well as the morphologies. By comparing the NO oxidation activities of sample with increased annealing temperature from 100 to 500 °C shown in Fig. 8, the GZC-300 sample (300 °C annealing) displayed the best NO conversion rate. It was due to the synergistic effect of suitable surface area with mesoporous structure, well crystal distribution onto the rGO conductive networks and the improved NO chemisorption on the oxygen vacancies by low temperature annealed Co-based metal oxides [70]. For the lower temperature treatment (100 and 200 °C), there was no enough energy for ZIF to be well oxidized to metal-oxides, which resulted in the extremely low contents of active semiconductor in the hybrids. With gradually increased temperature, the NO removal rate increased and got to the relative best at 300 °C. However, the much higher temperature could burn the rGO out, which hindered the electron transport and further resulted in the recombination of electron-holes during photocatalysis. In addition, the ZnCo_2O_4 crystals aggregated in the composites after high-temperature annealing, which can decrease the active surface area of photocatalysts. It could also result in the activity drop in NO removal.

In this photocatalytic system, NO could be oxidized by many

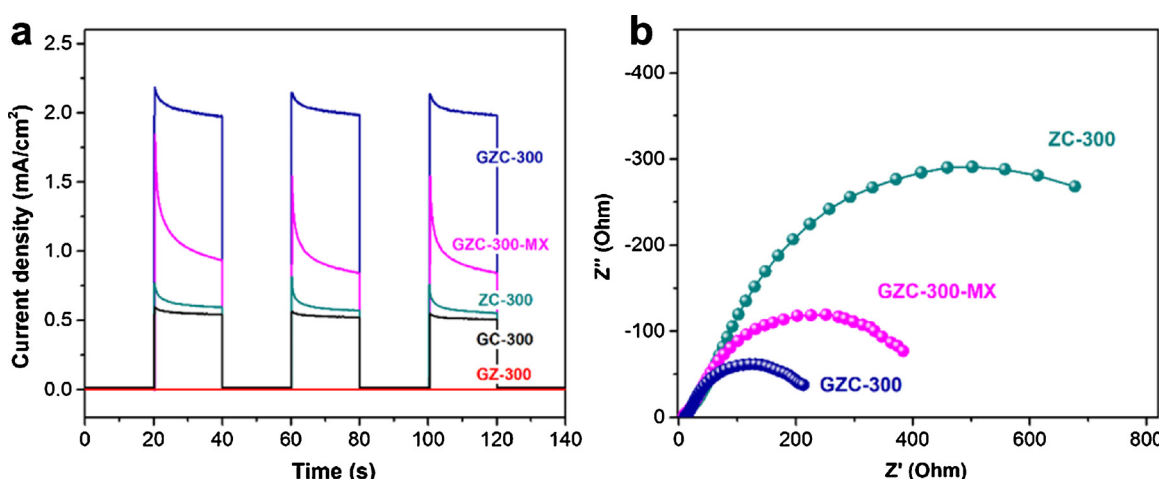


Fig. 7. (a) The transient photocurrent responses, (b) EIS spectra of different photocatalysts.

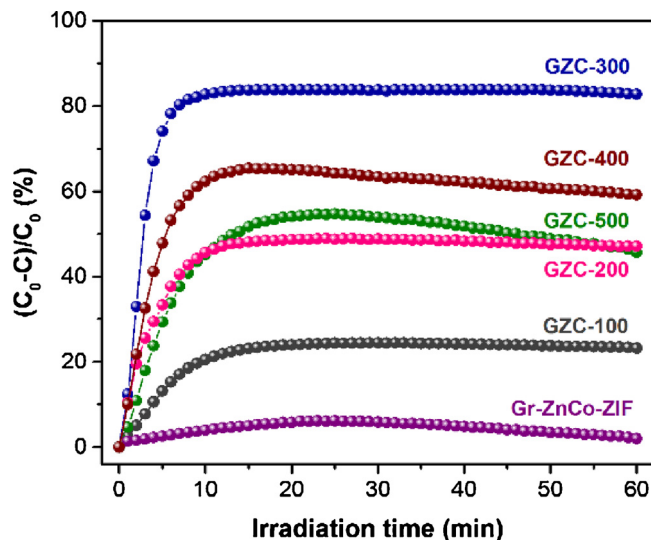
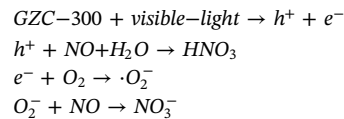


Fig. 8. Reaction profiles of photocatalytic NO oxidation under visible lights ($\lambda \geq 420$ nm) irradiation by adjusting the annealing temperature.

oxidizing species, such as photo-excited holes, superoxide radical ($\cdot\text{O}_2^-$) and hydroxyl radicals ($\cdot\text{OH}$). To understand the photocatalytic mechanism, a series active species trapping experiments were performed with the trapping agents of AgNO_3 for e^- , KI for h^+ , $\text{p}\text{-benzoquinone}$ (PBQ) for $\cdot\text{O}_2^-$ and $\text{tert}\text{-butyl alcohol}$ (TBA) for $\cdot\text{OH}$. As illustrated in Fig. 9a, $\cdot\text{OH}$ was not the active specie since the TBA treated sample displayed the similar activity like untreated GZC-300. This was due to its limited valence band position of 2.38 eV, which

could not reach the energy level of $\cdot\text{OH}/\text{H}_2\text{O}$ (2.80 eV) as the energy level diagram displayed in Fig. 9b. (The band structure was calculated by the Kubelka-Munk transformation from UV-vis and the flat band potential result from electrochemical test shown in Fig. S7.) On the contrast, with trapping photo-excited holes by KI , the catalyst was nearly deactivated indicating h^+ was the main active specie in this reaction by the direct oxidization of NO to NO_3^- with the existence of water. In addition, with the present of AgNO_3 and PBQ , the NO removal activities were slightly depressed suggesting that the photo-excited electron could be reacted with O_2 to produce $\cdot\text{O}_2^-$ with further oxidizing NO . To sum up, with the low conduction band energy (-0.32 eV) and high valence band energy (2.38 eV), the photocatalytic reaction formulas could be expressed as following and the photocatalytic mechanism was proposed in Fig. 9b:



As a well-recognized visible light photocatalyst, N-doped TiO_2 prepared by calcination of P25 TiO_2 in NH_3 was adopted as the reference to evaluate the photocatalytic performances of GZC-300. Fig. 10 demonstrated the long-term stability comparison of GZC-300 and N-doped TiO_2 in photocatalytic NO oxidation irradiated with both solar light and visible light ($\lambda \geq 420$ nm) for more than 24 h. In the first hour, the N- TiO_2 as well as GZC-300 presented high NO conversion of approximately $\sim 90\%$ for solar light and $\sim 80\%$ for visible light. After that, the conversion of N- TiO_2 decreased gradually, especially under visible-light irradiation, which dropped to 65.9% (solar light) and 39.3% (visible light), respectively. On the contrast, the GZC-300 showed an extremely high stability by retaining $\sim 90\%$ degradation of

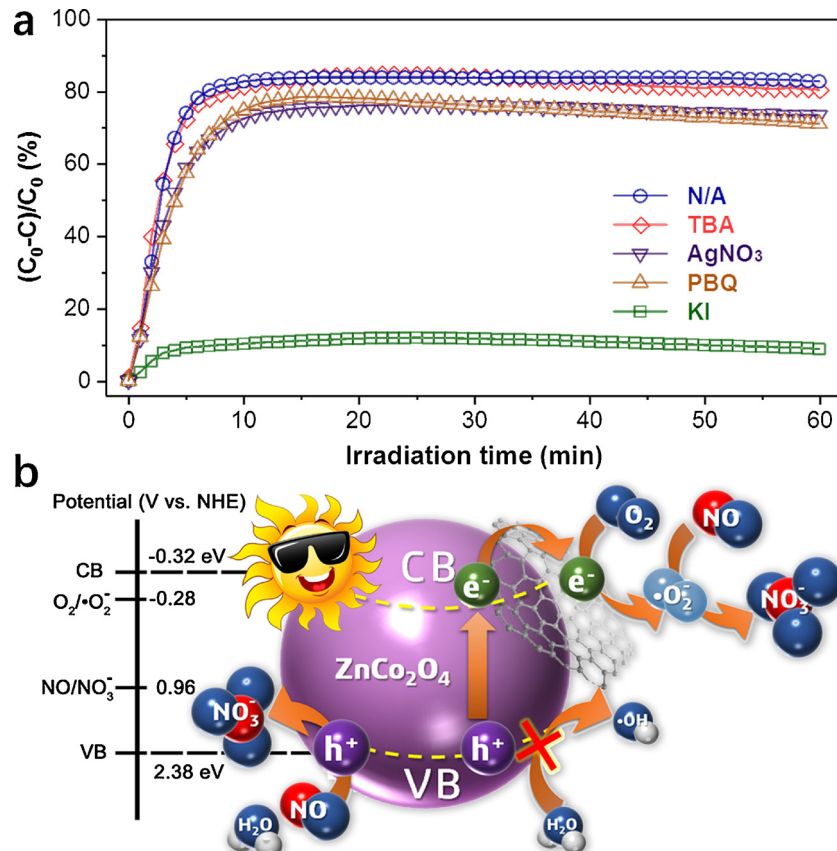


Fig. 9. (a) Comparison of photocatalytic activities of GZC-300 by different treatment to trap active species under visible light irradiation. (b) Possible photocatalytic mechanism of GZC-300 in visible-light driven NO oxidation.

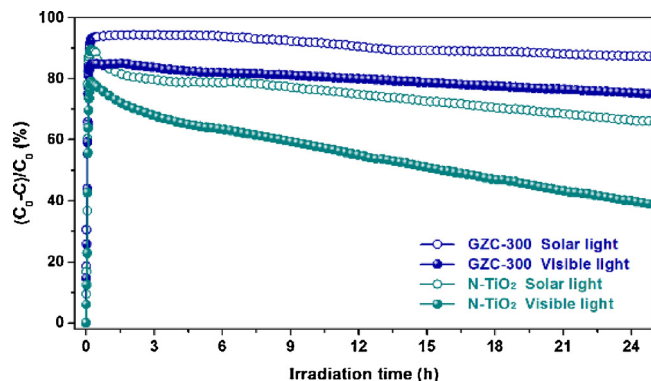


Fig. 10. Long-term stability comparison of GZC-300 and N-doped TiO_2 in photocatalytic NO oxidation irradiated with both solar light and visible light ($\lambda \geq 420 \text{ nm}$), respectively.

NO after 24 h, which is due to the stable mesoporous structure and suitable Zn/Co ratio inhibiting the light corrosive and structure destruction of the photocatalysts. Thus, the as-prepared GZC-300 sample could be used as air-purification catalyst and showed its potential applications in environmental fields.

4. Conclusion

In summary, we have successfully synthesized a novel mesocrystal ZnCo_2O_4 on rGO catalyst by the low temperature calcination of bimetal ZIF/rGO precursors. By carefully adjusting the rGO components, Zn/Co ratio and the annealing temperature, the optimized material shows an enhanced NO removal of 83.8% under visible light ($\lambda \geq 420 \text{ nm}$) and 92.6% under solar light. Active species trapping tests confirm the photo-excited holes and $\cdot\text{O}_2^-$ are the oxidizer for NO oxidation. Comparing with N-doped TiO_2 , as prepared rGO@ ZnCo_2O_4 reveals a much more stable and superior photocatalytic activity, making it a promising catalyst for gas-phase pollutant removal in environmental purification.

Acknowledgements

Authors acknowledge the financial support from National Natural Science Foundation of China (NSFC 21761142011, 91645102, 51502174), PCSIRT (IRT1269), Singapore National Research Foundation under the grant of NRF2017NRF-NSFC001-007, China Postdoctoral Science Foundation (2018M630981), Shenzhen Peacock Plan (Grant No. 827-000113, KQTD2016053112042971) and the Educational Commission of Guangdong Province (2016KCXTD006 and 2016KSTCX126).

Appendix A. Supplementary data

Supplementary material related to this article can be found, in the online version, at doi:<https://doi.org/10.1016/j.apcatb.2018.05.033>.

References

- H. Akimoto, Global air quality and pollution, *Science* 302 (2003) 1716–1719.
- S. Xiao, D. Zhang, G. Li, H. Li, Development of Advanced Nanoarchitectures for Photocatalytic Treatment of NO_x , *Nanostructured Photocatalysts*, Springer, Cham, 2016, pp. 99–124.
- Z. Zhao, R. Yu, R. Zhao, C. Shi, H. Gies, F.-S. Xiao, D. De Vos, T. Yokoi, X. Bao, U. Kolb, M. Feyen, R. McGuire, S. Maurer, A. Moini, U. Mueller, W. Zhang, Cu-exchanged Al-rich SSZ-13 zeolite from organotemplate-free synthesis as NH_3 -SCR catalyst: effects of Na^+ ions on the activity and hydrothermal stability, *Appl. Catal. B: Environ.* 217 (2017) 421–428.
- M. Salazar, S. Hoffmann, L. Tillmann, V. Singer, R. Becker, W. Gruenert, Hybrid catalysts for the selective catalytic reduction (SCR) of NO by NH_3 : precipitates and physical mixtures, *Appl. Catal. B: Environ.* 218 (2017) 793–802.
- C. Paolucci, I. Khurana, A.A. Parekh, S. Li, A.J. Shih, H. Li, J.R. Di Iorio, J.D. Albaracin-Caballero, A. Yezerski, J.T. Miller, W.N. Delgass, F.H. Ribeiro, W.F. Schneider, R. Gounder, Dynamic multinuclear sites formed by mobilized copper ions in NO_x selective catalytic reduction, *Science* 357 (2017) 898.
- D. Meng, Q. Xu, Y. Jiao, Y. Guo, L. Wang, G. Lu, W. Zhan, Spinel structured CoAlNbO_x mixed oxide catalyst for the selective catalytic reduction of NO_x with NH_3 , *Appl. Catal. B: Environ.* 221 (2018) 652–663.
- A. Marberger, D. Ferri, M. Elsener, A. Sagar, C. Artner, K. Schermanz, O. Krocher, Relationship between structures and activities of supported metal vanadates for the selective catalytic reduction of NO by NH_3 , *Appl. Catal. B: Environ.* 218 (2017) 731–742.
- P.G.W.A. Kompio, A. Brueckner, F. Hipler, O. Manoylova, G. Auer, G. Mestl, W. Gruenert, $\text{V}_{2}\text{O}_5\text{-WO}_3\text{/TiO}_2$ catalysts under thermal stress: responses of structure and catalytic behavior in the selective catalytic reduction of NO by NH_3 , *Appl. Catal. B: Environ.* 217 (2017) 365–377.
- M. Bendrich, A. Scheuer, R.E. Hayes, M. Votsmeier, Unified mechanistic model for standard SCR, fast SCR, and NO_2 SCR over a copper chabazite catalyst, *Appl. Catal. B: Environ.* 222 (2018) 76–87.
- T. Yao, Y.F. Duan, Z.Z. Yang, Y. Li, L.W. Wang, C. Zhu, Q. Zhou, J. Zhang, M. She, M. Liu, Experimental characterization of enhanced SNCR process with carbonaceous gas additives, *Chemomet. Intell. Lab. Syst.* 177 (2017) 149–156.
- H. Chen, D.Z. Chen, S. Fan, L. Hong, D. Wang, SNCR de-nox within a moderate temperature range using urea-spiked hydrazine hydrate as reductant, *Chemomet. Intell. Lab. Syst.* 161 (2016) 208–218.
- J.D. Felix, E.M. Elliott, S.L. Shaw, Nitrogen isotopic composition of coal-fired power plant NO_x : influence of emission controls and implications for global emission inventories, *Environ. Sci. Technol.* 46 (2012) 3528–3535.
- J.C.C. Yu, V.H. Nguyen, J. Lasek, J.C.S. Wu, Titania nanosheet photocatalysts with dominantly exposed (001) reactive facets for photocatalytic NO_x abatement, *Appl. Catal. B: Environ.* 219 (2017) 391–400.
- Y. Nosaka, A.Y. Nosaka, Generation and detection of reactive oxygen species in photocatalysis, *Chem. Rev.* 117 (2017) 11302–11336.
- J.M. Luo, G.H. Dong, Y.Q. Zhu, Z. Yang, C.Y. Wang, Switching of semiconducting behavior from n-type to p-type induced high photocatalytic NO removal activity in $\text{g-C}_3\text{N}_4$, *Appl. Catal. B: Environ.* 214 (2017) 46–56.
- J.D. Hu, D.Y. Chen, N.J. Li, Q.F. Xu, H. Li, J.H. He, J.M. Lu, In situ fabrication of $\text{Bi}_2\text{O}_3\text{CO}_3\text{/MoS}_2$ on carbon nanofibers for efficient photocatalytic removal of NO under visible-light irradiation, *Appl. Catal. B: Environ.* 217 (2017) 224–231.
- J. Lasek, Y.-H. Yu, J.C. Wu, Removal of NO_x by photocatalytic processes, *J. Photoch. Photobiol. C* 14 (2013) 29–52.
- I. Nakamura, N. Negishi, S. Kutsuna, T. Ihara, S. Sugihara, E. Takeuchi, Role of oxygen vacancy in the plasma-treated TiO_2 photocatalyst with visible light activity for NO removal, *J. Mol. Catal. A-Chem.* 161 (2000) 205–212.
- Q.P. Wu, R. van de Krol, Selective photoreduction of nitric oxide to nitrogen by nanostructured TiO_2 photocatalysts: role of oxygen vacancies and iron dopant, *J. Am. Chem. Soc.* 134 (2012) 9369–9375.
- D.Q. Zhang, M.C. Wen, S.S. Zhang, P.J. Liu, W. Zhu, G.S. Li, H.X. Li, Au nanoparticles enhanced rutile TiO_2 nanorod bundles with high visible-light photocatalytic performance for NO oxidation, *Appl. Catal. B: Environ.* 147 (2014) 610–616.
- J. Ma, H. Wu, Y. Liu, H. He, Photocatalytic removal of NO_x over visible light responsive oxygen-deficient TiO_2 , *J. Phys. Chem. C* 118 (2014) 7434–7441.
- M.C. Wen, P.J. Liu, S. Xiao, K. Mori, Y. Kuwahara, H. Yamashita, H.X. Li, D.Q. Zhang, Uniform anatase single-crystal cubes with high thermal stability fully enclosed by active {010} and {001} facets, *Rsc Adv.* 5 (2015) 11029–11035.
- W. Zhu, S.N. Xiao, D.Q. Zhang, P.J. Liu, H.J. Zhou, W.R. Dai, F.F. Liu, H.X. Li, Highly efficient and stable Au/ $\text{CeO}_2\text{-TiO}_2$ photocatalyst for nitric oxide abatement: potential application in flue gas treatment, *Langmuir* 31 (2015) 10822–10830.
- F. Dong, Q.Y. Li, Y. Zhou, Y.J. Sun, H.D. Zhang, Z.B. Wu, In situ decoration of plasmonic Ag nanocrystals on the surface of $(\text{BiO})_2\text{CO}_3$ hierarchical microspheres for enhanced visible light photocatalysis, *Dalton Trans.* 43 (2014) 9468–9480.
- Y.J. Sun, T. Xiong, Z.L. Ni, J. Liu, F. Dong, W. Zhang, W.K. Ho, Improving $\text{g-C}_3\text{N}_4$ photocatalysis for NO_x removal by Ag nanoparticles decoration, *Appl. Surf. Sci.* 358 (2015) 356–362.
- Z.B. Wu, F. Dong, Y. Liu, H.Q. Wang, Enhancement of the visible light photocatalytic performance of C-doped TiO_2 by loading with V_{2}O_5 , *Catal. Commun.* 11 (2009) 82–86.
- Q.Y. Li, H.T. Liu, F. Dong, M. Fu, Hydrothermal formation of N-doped $(\text{BiO})_2\text{CO}_3$ honeycomb-like microspheres photocatalysts with bismuth citrate and dicyandiamide as precursors, *J. Colloid. Interf. Sci.* 408 (2013) 33–42.
- F. Dong, Y.J. Sun, M. Fu, W.K. Ho, S.C. Lee, Z.B. Wu, Novel in situ N-Doped $(\text{BiO})_2\text{CO}_3$ hierarchical microspheres self-assembled by nanosheets as efficient and durable visible light driven photocatalyst, *Langmuir* 28 (2012) 766–773.
- Y. Zhou, X.J. Zhang, Q. Zhang, F. Dong, F. Wang, Z. Xiong, Role of graphene on the band structure and interfacial interaction of Bi_2WO_6 /graphene composites with enhanced photocatalytic oxidation of NO, *J. Mater. Chem. A* 2 (2014) 16623–16631.
- A. Trapalis, N. Todorova, T. Giannakopoulou, N. Boukos, T. Speliotis, D. Dimotikali, J.G. Yu, TiO_2 /graphene composite photocatalysts for NO_x removal: a comparison of surfactant-stabilized graphene and reduced graphene oxide, *Appl. Catal. B: Environ.* 180 (2016) 637–647.
- N. Todorova, T. Giannakopoulou, S. Karapati, D. Petridis, T. Vaimakis, C. Trapalis, Composite TiO_2 /clays materials for photocatalytic NO_x oxidation, *Appl. Surf. Sci.* 319 (2014) 113–120.
- X. Song, Y. Hu, M.M. Zheng, C.H. Wei, Solvent-free in situ synthesis of $\text{g-C}_3\text{N}_4\text{/}$ {001} TiO_2 composite with enhanced UV- and visible-light photocatalytic activity

for NO oxidation, *Appl. Catal. B: Environ.* 182 (2016) 587–597.

[33] Y.H. Li, K.L. Lv, W.K. Ho, F. Dong, X.F. Wu, Y. Xia, Hybridization of rutile TiO_2 (rTiO_2) with $\text{g-C}_3\text{N}_4$ quantum dots (CN QDs): an efficient visible-light-driven z-scheme hybridized photocatalyst, *Appl. Catal. B: Environ.* 202 (2017) 611–619.

[34] N. Tian, H.W. Huang, C.Y. Liu, F. Dong, T.R. Zhang, X. Du, S.X. Yu, Y.H. Zhang, In situ co-pyrolysis fabrication of $\text{CeO}_2/\text{g-C}_3\text{N}_4$ n-n type heterojunction for synchronously promoting photo-induced oxidation and reduction properties, *J. Mater. Chem. A* 3 (2015) 17120–17129.

[35] F. Dong, Z.W. Zhao, T. Xiong, Z.L. Ni, W.D. Zhang, Y.J. Sun, W.K. Ho, In situ construction of $\text{g-C}_3\text{N}_4/\text{g-C}_3\text{N}_4$ metal-free heterojunction for enhanced visible-light photocatalysis, *ACS Appl. Mater. Inter.* 5 (2013) 11392–11401.

[36] F. Dong, Z.W. Zhao, Y.J. Sun, Y.X. Zhang, S. Yan, Z.B. Wu, An advanced semimetal-organic bi Spheres- $\text{g-C}_3\text{N}_4$ nanohybrid with SPR-Enhanced visible-light photocatalytic performance for NO purification, *Environ. Sci. Technol.* 49 (2015) 12432–12440.

[37] G.S. Li, B. Jiang, S.N. Xiao, Z.C. Lian, D.Q. Zhang, J.C. Yu, H.X. Li, An efficient dye-sensitized BiOCl photocatalyst for air and water purification under visible light irradiation, *Environ. Sci. Proc. Impacts* 16 (2014) 1975–1980.

[38] G.S. Li, D.Q. Zhang, J.C. Yu, M.K.H. Leung, An efficient bismuth tungstate visible-light-driven photocatalyst for breaking down nitric oxide, *Environ. Sci. Technol.* 44 (2010) 4276–4281.

[39] G.S. Li, D.Q. Zhang, J.C. Yu, Ordered mesoporous BiVO_4 through nanocasting: a superior visible light-driven photocatalyst, *Chem. Mater.* 20 (2008) 3983–3992.

[40] T. Xiong, M.Q. Wen, F. Dong, J.Y. Yu, L.L. Han, B. Lei, Y.X. Zhang, X.S. Tang, Z.G. Zang, Three dimensional Z-scheme $(\text{BiO})_2\text{CO}_3/\text{MoS}_2$ with enhanced visible light photocatalytic NO removal, *Appl. Catal. B: Environ.* 199 (2016) 87–95.

[41] G.H. Zhang, S.C. Hou, H. Zhang, W. Zeng, F.L. Yan, C.C. Li, H.G. Duan, High-performance and ultra-stable lithium-ion batteries based on MOF-derived ZnO/ZnO quantum Dots/C core-shell nanorod arrays on a carbon cloth anode, *Adv. Mater.* 27 (2015) 2400–2405.

[42] S.J. Yang, S. Nam, T. Kim, J.H. Im, H. Jung, J.H. Kang, S. Wi, B. Park, C.R. Park, Preparation and exceptional lithium anodic performance of porous carbon-coated ZnO quantum dots derived from a metal-organic framework, *J. Am. Chem. Soc.* 135 (2013) 7394–7397.

[43] W. Xia, A. Mahmood, R.Q. Zou, Q. Xu, Metal-organic frameworks and their derived nanostructures for electrochemical energy storage and conversion, *Energy Environ. Sci.* 8 (2015) 1837–1866.

[44] N.L. Rosi, J. Eckert, M. Eddaoudi, D.T. Vodak, J. Kim, M. O'Keeffe, O.M. Yaghi, Hydrogen storage in microporous metal-organic frameworks, *Science* 300 (2003) 1127–1129.

[45] H. Furukawa, K.E. Cordova, M. O'Keeffe, O.M. Yaghi, The chemistry and applications of metal-organic frameworks, *Science* 341 (2013) 974.

[46] J.R. Li, R.J. Kuppler, H.C. Zhou, Selective gas adsorption and separation in metal-organic frameworks, *Chem. Soc. Rev.* 38 (2009) 1477–1504.

[47] W. Xia, R.Q. Zou, L. An, D.G. Xia, S.J. Guo, A metal-organic framework route to in situ encapsulation of $\text{Co}@\text{Co}_3\text{O}_4@\text{C}$ core@bisphere nanoparticles into a highly ordered porous carbon matrix for oxygen reduction, *Energy Environ. Sci.* 8 (2015) 568–576.

[48] X.J. Wang, H.G. Zhang, H.H. Lin, S. Gupta, C. Wang, Z.X. Tao, H. Fu, T. Wang, J. Zheng, G. Wu, X.G. Li, Directly converting Fe-doped metal organic frameworks into highly active and stable Fe-N-C catalysts for oxygen reduction in acid, *Nano Energy* 25 (2016) 110–119.

[49] Z.H. Li, M.F. Shao, L. Zhou, R.K. Zhang, C. Zhang, M. Wei, D.G. Evans, X. Duan, Directed growth of metal-organic frameworks and their derived carbon-based network for efficient electrocatalytic oxygen reduction, *Adv. Mater.* 28 (2016) 2337–2344.

[50] J. Lee, O.K. Farha, J. Roberts, K.A. Scheidt, S.T. Nguyen, J.T. Hupp, Metal-organic framework materials as catalysts, *Chem. Soc. Rev.* 38 (2009) 1450–1459.

[51] W.W. Zhan, Q. Kuang, J.Z. Zhou, X.J. Kong, Z.X. Xie, L.S. Zheng, Semiconductor@Metal-organic framework core-shell heterostructures: a case of $\text{ZnO}@\text{ZIF-8}$ nanorods with selective photoelectrochemical response, *J. Am. Chem. Soc.* 135 (2013) 1926–1933.

[52] J.X. Xu, J.Y. Gao, C. Wang, Y. Yang, L. Wang, $\text{NH}_2\text{-MIL-125(TO)}$ /graphitic carbon nitride heterostructure decorated with NiPd co-catalysts for efficient photocatalytic hydrogen production, *Appl. Catal. B: Environ.* 219 (2017) 101–108.

[53] W. Zhu, P.J. Liu, S.N. Xiao, W.C. Wang, D.Q. Zhang, H.X. Li, Microwave-assisted synthesis of Ag-doped MOFs-like organotitanium polymer with high activity in visible-light driven photocatalytic NO oxidation, *Appl. Catal. B: Environ.* 172 (2015) 46–51.

[54] J. Yang, F. Zhang, H. Lu, X. Hong, H. Jiang, Y. Wu, Y. Li, Hollow $\text{Zn}/\text{Co ZIF}$ particles derived from core-shell $\text{zif-67}@\text{zif-8}$ as selective catalyst for the semi-hydrogenation of acetylene, *Angew. Chem. Int. Ed.* 127 (2015) 11039–11043.

[55] J. Zhang, J.G. Yu, M. Jaroniec, J.R. Gong, Noble metal-free reduced graphene Oxide- $\text{Zn}_x\text{Cd}_{1-x}\text{S}$ nanocomposite with enhanced solar photocatalytic H_2 -production performance, *Nano Lett.* 12 (2012) 4584–4589.

[56] Q.J. Xiang, J.G. Yu, M. Jaroniec, Synergistic effect of MoS_2 and graphene as cocatalysts for enhanced photocatalytic H_2 production activity of TiO_2 nanoparticles, *J. Am. Chem. Soc.* 134 (2012) 6575–6578.

[57] X.J. Bai, L. Wang, Y.F. Zhu, Visible photocatalytic activity enhancement of ZnWO_4 by graphene hybridization, *ACS Catal.* 2 (2012) 2769–2778.

[58] T.G. Xu, L.W. Zhang, H.Y. Cheng, Y.F. Zhu, Significantly enhanced photocatalytic performance of ZnO via graphene hybridization and the mechanism study, *Appl. Catal. B: Environ.* 101 (2011) 382–387.

[59] M. Lan, R.-M. Guo, Y. Dou, J. Zhou, A. Zhou, J.-R. Li, Fabrication of porous pt-doping heterojunctions by using bimetallic MOF template for photocatalytic hydrogen generation, *Nano Energy* 33 (2017) 238–246.

[60] X. Tang, J.-H. Zhao, Y.-H. Li, Z.-J. Zhou, K. Li, F.-T. Liu, Y.-Q. Lan, Co-Doped $\text{Zn}_{1-x}\text{Cd}_x\text{S}$ nanocrystals from metal-organic framework precursors: porous micro-structure and efficient photocatalytic hydrogen evolution, *Dalton Trans.* 46 (2017) 10553–10557.

[61] Q. Zhou, Q. Zhao, W. Xiong, X. Li, J. Li, L. Zeng, Hollow porous zinc cobaltate nanocubes photocatalyst derived from bimetallic zeolitic imidazolate frameworks towards enhanced gaseous toluene degradation, *J. Colloid Interf. Sci.* (2018).

[62] S. Xiao, D. Pan, L. Wang, Z. Zhang, Z. Lyu, W. Dong, X. Chen, D. Zhang, W. Chen, H. Li, Porous CuO nanotubes/graphene with sandwich architecture as high-performance anodes for lithium-ion batteries, *Nanoscale* 8 (2016) 19343–19351.

[63] Q. Li, X. Li, S. Wageh, A.A. Al-Ghamdi, J.G. Yu, $\text{CdS}/\text{Graphene}$ nanocomposite photocatalysts, *Adv. Energy Mater.* 5 (2015) 1500010.

[64] X.J. Bai, C.P. Sun, D. Liu, X.H. Luo, D. Li, J. Wang, N.X. Wang, X.J. Chang, R.L. Zong, Y.F. Zhu, Photocatalytic degradation of deoxyribofuranose using graphene/ ZnO hybrids in aqueous suspension, *Appl. Catal. B: Environ.* 204 (2017) 11–20.

[65] J. Rosen, G.S. Hutchings, F. Jiao, Ordered mesoporous cobalt oxide as highly efficient oxygen evolution catalyst, *J. Am. Chem. Soc.* 135 (2013) 4516–4521.

[66] X.X. Chang, T. Wang, P. Zhang, J.J. Zhang, A. Li, J.L. Gong, Enhanced surface reaction kinetics and charge separation of p-n heterojunction $\text{Co}_3\text{O}_4/\text{BiVO}_4$ photo-anodes, *J. Am. Chem. Soc.* 137 (2015) 8356–8359.

[67] S. Wang, Z. Ding, X. Wang, A stable ZnCo_2O_4 cocatalyst for photocatalytic CO_2 reduction, *Chem. Commun.* 51 (2015) 1517–1519.

[68] K. Goswami, R. Ananthakrishnan, S. Mandal, Facile synthesis of cation doped $\text{ZnO-ZnCo}_2\text{O}_4$ hetero-nanocomposites for photocatalytic decomposition of aqueous organics under visible light, *Mater. Chem. Phys.* 206 (2018) 174–185.

[69] Y. Dou, J. Zhou, A. Zhou, J.-R. Li, Z. Nie, Visible-light responsive MOF encapsulation of noble-metal-sensitized semiconductors for high-performance photoelectrochemical water splitting, *J. Mater. Chem. A* 5 (2017) 19491–19498.

[70] X. Xie, Y. Li, Z.-Q. Liu, M. Haruta, W. Shen, Low-temperature oxidation of CO catalysed by Co_3O_4 nanorods, *Nature* 458 (2009) 746.